

Tuneable large nonlinear charge transport driven by the quantum metric at room temperatures in TbMn_6Sn_6

Weiyao Zhao^{1, 8}, Kaijian Xing^{2, 8}, Yufei Zhao^{3, 8}, Lei Chen⁴, Min Hong⁴, Yuefeng Yin¹, Yang Liu⁵,
Khoa Dang Le⁶, Jacob Gayles⁶, Fang Tang⁷, Yong Fang⁷, Binghai Yan³, and Julie Karel^{1*}

¹ *Department of Materials Science & Engineering, & ARC Centre of Excellence in Future Low-Energy Electronics Technologies, Monash University, Clayton VIC 3800, Australia*

² *School of Physics & Astronomy, Monash University, Clayton VIC 3800, Australia*

³ *Department of Condensed Matter Physics, Weizmann Institute of Science, Rehovot 7610001, Israel*

⁴ *Centre for Future Materials, University of Southern Queensland, Springfield QLD 4300, Australia*

⁵ *Monash Centre for Electron Microscopy, Monash University, Clayton VIC 3800, Australia*

⁶ *Department of Physics, University of South Florida, Tampa, FL 33620, USA*

⁷ *Jiangsu Laboratory of Advanced Functional Materials, Changshu Institute of Technology, Changshu 215500, China*

⁸ *The authors contribute equally to this work.*

Nonlinear electrodynamics in materials manifests as an electronic response that depends on second- or higher-order powers of the applied electromagnetic field. This response is highly dependent on the underlying crystal symmetries in the material and is typically smaller than the linear responses. Nonlinear responses are therefore usually employed to expose the symmetry breaking, geometric properties of the electronic band structure in materials. Naturally, a material system with a strong nonlinear response is also the key component in nonlinear devices. Here we report the strong room-temperature second-harmonic transport response in a quantum magnet, TbMn_6Sn_6 , which is governed by the quantum metric and can be tuned with applied magnetic fields and temperature. We show that around room temperature, which is close to the spontaneous spin-reorientation transition, the magnetic configurations, and therefore the related symmetry breaking phases, are easily controlled. Our results pave the way from quantum materials to high performance tuneable nonlinear device applications at room temperature.

* julie.karel@monash.edu

Nonlinear responses, e.g., high-harmonic electric/optical generation, in quantum materials have been employed to trigger promising applications such as rectification and terahertz detection(1-4). Nonlinear transport provides valuable insight into the intricate quantum geometry in condensed matter physics(5, 6). In momentum space, the real and imaginary part of the quantum geometry defines the metric and curvature of Bloch wavefunctions, respectively. For example, in non-magnetic WTe₂ flakes, the nonlinear anomalous Hall effect has been shown to result from the asymmetric distribution of the Berry curvature dipole (D_{BC}) (7); in even-layer antiferromagnetic MnBi₂Te₄ thin flakes, the quantum metric dipole (D_{metric}) gives rise to both transverse and longitudinal nonreciprocal responses below 24 K (8, 9). The second-order conductivity induced by D_{BC} and D_{metric} have even and odd time-reversal symmetry (\hat{T}) dependence, respectively, and therefore will contribute to different parabolic I-V responses, as sketched in Fig. 1A.(10) Moreover, it has also been demonstrated in chiral crystals that the bilinear response is associated with electric magneto-chiral anisotropy (eMChA)(11), described by $R(I, B) = R_0(1 + \mu^2 B^2 + \gamma^\pm B \cdot I)$ and presented in Fig. 1A.

To display a second-order signal $\mathcal{J}_k^{(2)} = \sigma^{(2)} E_i E_j$, inversion and related mirror symmetries must be broken such that the voltage response does not invert when reversing the applied current. Hence, the second-order response is also an excellent tool to probe hidden symmetry-breaking phases. One prime example is the charge-ordered Kagome metal CsV₃Sb₅, which is generally viewed with a centrosymmetric lattice distortion ($T_{\text{CDW}} = 94$ K) but exhibits chiral and time-reversal asymmetric quasi-particle interference(12-14). A second-harmonic signal as well as eMChA is observed below 35 K(12), indicating the possible presence of orbital loop currents, which spontaneously lowering symmetry. In MnBi₂Te₄ and CsV₃Sb₅, while the nonlinear response can be manipulated by an external magnetic field, it only survives at low temperatures (8, 9), which is of limited use in practical device applications.

In this work, we report unexpected second order nonlinear electronic transport at room temperature in the centrosymmetric magnet TbMn₆Sn₆, which holds rich magnetic interactions. The response has a complicated temperature dependence driven by the spin-reorientation transition around room temperature (e.g., 270 – 330 K) (15, 16). More importantly, we show that the field-dependent D_{metric} is tuneable via controlling the magnetic configuration and is accompanied by a relatively-large field-independent response. Our results pave the way for nonlinear device design based on quantum magnets operating at room temperature.

The magnetic phases in TbMn₆Sn₆ Modifying the symmetry in a quantum material is one of the most important routes to manifesting sizeable D_{BC} and D_{metric} -induced nonlinear physics, such as that observed in artificially corrugated bilayer graphene.(17-20) An alternative approach in nonlinear responses is to introduce magnetic order in a triangular lattice with in-plane antiferromagnetism to break the symmetries. The kagome magnet system, such as the RMn_6Sn_6 family, where R is a rare earth element, is a promising candidate for locating this magnetism-induced symmetry-breaking behaviour. RMn_6Sn_6 compounds crystallize in a $HfFe_6Ge_6$ -type structure (centrosymmetric space group $P6/mmm$), which possesses Mn kagome layers stacked along the c axis. In each unit cell, the R atoms occupy the honeycomb centres between two Mn layers. Except for the case of a nonmagnetic R (Y and Lu) atom, the competing magnetic interactions, namely direct Mn-Mn exchange, indirect $4f$ - $3d$ type R -Mn exchange and Ruderman-Kittel-Kasuya-Yosida (RKKY) type R - R interactions, contribute to rather complicated magnetic structures, offering a rich field for nonlinear physics. Among these magnetic interactions, intralayer Mn-Mn interactions are the strongest, and therefore ferromagnetic coupling within the kagome planes dominates. The hybridization between Mn $3d$ and R $5d$ orbitals always favours antiparallel alignment, thus yielding a negative exchange coupling between Mn and R (21). As a result, various magnetic structures have been observed, such as an easy- ab -plane anisotropy in $GdMn_6Sn_6$, an easy- c -axis anisotropy in $TbMn_6Sn_6$ and conical order in $DyMn_6Sn_6$ and $HoMn_6Sn_6$ (22). Particularly, in $TbMn_6Sn_6$, the ferrimagnetic ordering forms below $T_C \sim 420$ K, with both Tb and Mn magnetic moments aligned parallel/antiparallel to the a -axis, and, a spin reorientation occurs at $T_{SR} \sim 315$ K, where the moments rotate into the c -axis with a slight canting angle, as shown in Fig. 1B, (more SR transition sketch and related magnetization measurements are available in Figs. S1 & S2). The canting effect is verified in magnetization measurements shown in Fig. S2. Moreover, the magnetization does not saturate at high magnetic field, and the in-plane and out-of-plane magnetic moments at 5T and 300K are different, e.g., $5.19 \mu_B/f. u.$ and $5.25 \mu_B/f. u.$. These results confirm the robust canting ferrimagnetic ordering and in-plane moment components at room temperature. The magnetic ordering in the kagome lattice contributes to large Berry curvature in the material, which leads to a giant anomalous Nernst effect(23) and anomalous Hall effect(22) at around room temperature (15, 22-34). On top of this, inelastic neutron scattering (INS) results(15, 16, 31) indicate that the Mn in-plane spin configuration of the kagome lattice has features of ferromagnetism, flat-band antiferromagnetism, and chiral antiferromagnetism (Fig. 1B). Importantly for this work, the flat-band type antiferromagnetic spin structure in the Mn kagome lattice result in breaking of inversion symmetry (\hat{P}) and time-

reversal symmetry (\hat{T}), precisely the conditions necessary to observe the rarely explored quantum metric physics.

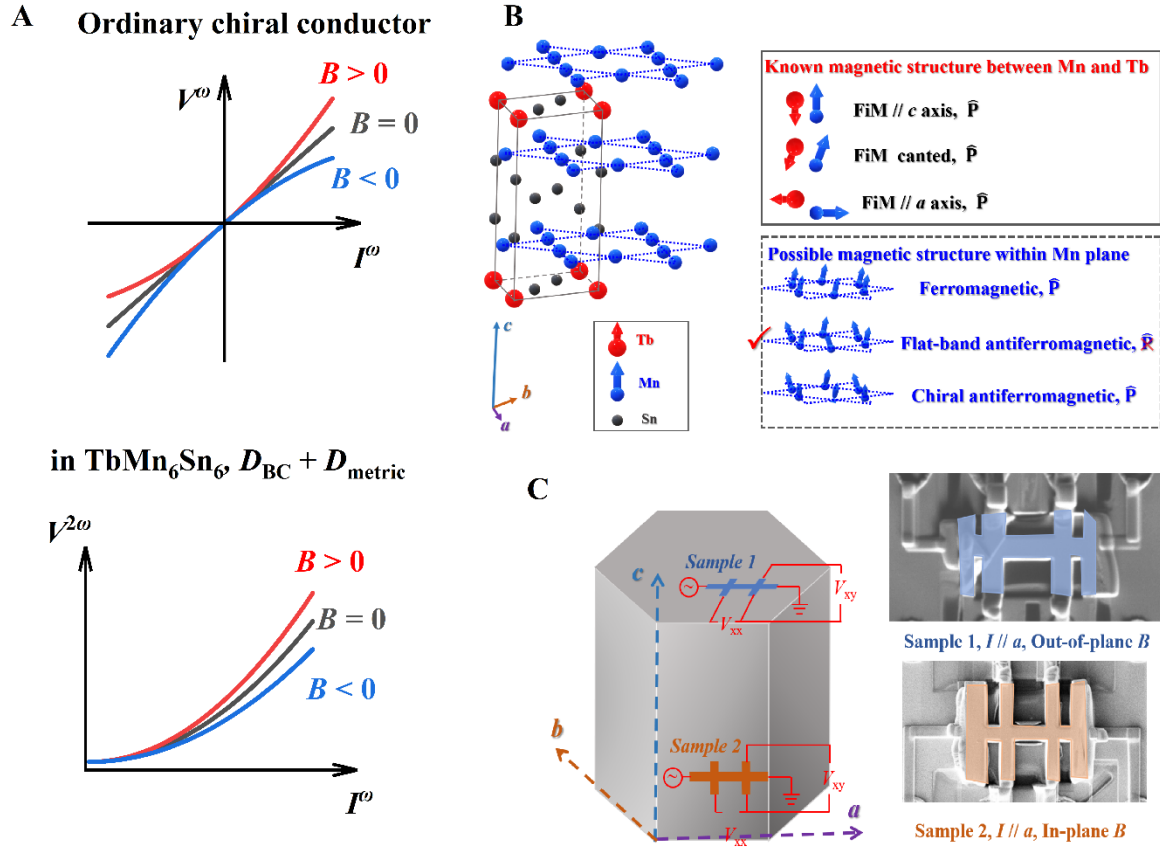


Fig. 1 (A) The nonlinear magnetoelectric responses, in (top) first order, e.g., a chiral conductor showing electric magneto-chiral anisotropy in applied magnetic fields, and (bottom) second order, e.g., the parabolic second-harmonic I-V curves show magnetic field dependence due to the quantum metric and Berry curvature dipole contributions. The second-order conductivity induced by D_{BC} and D_{metric} have even and odd time-reversal symmetry (\hat{T}) dependence, respectively, therefore will contribute to different parabolic I-V responses. (B) In the quantum magnet TbMn_6Sn_6 , alternative stacking of kagome lattice Mn layers and honeycomb lattice Tb layers form ferrimagnetic ordering. The temperature dependent ferrimagnetic orders are sketched in solid-line box between two sublattices, which is the well-known magnetic configuration. Note that, the middle configuration in the solid box shows room-temperature magnetic moments' orientation for Mn and Tb, in which the tilting angle is slightly exaggerated [$\sim 13^\circ$ at 300 K(24)] for a clearer demonstration of the tilting effect. The “hidden” local spin texture of the Mn-kagome plane are sketched in the dash-line box, which are the possible local structures as verified by INS(16), in which the so-called “flat-band antiferromagnetic” in-plane components break the inversion symmetry in the Mn-kagome plane. Thus, the quantum metric dipole is nonzero due to the broken time-reversal (\hat{T}) and inversion (\hat{P}) symmetries. (C) The demonstration of focused-ion beam (FIB) fabrication devices in TbMn_6Sn_6 crystal. Both samples have current flowing

along the a axis, while the orientation of applied fields are along the out-of-plane (c axis) direction and within the basal plane ($[\bar{1}\bar{2}0]$ direction), respectively.

Electronic transport properties of TbMn₆Sn₆ The anisotropic magnetotransport properties of TbMn₆Sn₆ with applied field along the c axis or the basal plane ($[\bar{1}\bar{2}0]$ direction) for Sample 1 and Sample 2 (see Fig. 1C for sample orientation), respectively, have been studied (Figs. S3 & S4), indicating the excellent crystal quality of the studied devices. Figs. 2A & B demonstrates the first-order transport results at 300 K. The negative magnetoresistance (MR) in Sample 1 is sharper at low fields, where the moments are not fully aligned, and shows linear dependency with fields above the alignment, indicating spin-disorder-scattering and electron-magnon scattering, respectively(35). With applied in plane fields, a field-induced SR occurs, and shows a U-shape positive MR in the SR region, similar to the reports in the Fe₃Sn₂ kagome magnet(36). A giant anomalous Hall effect arising from the large Berry curvature of the massive Dirac fermions has been reported up to room temperature(33), and is also observed in Samples 1 & 2, as shown in Fig. 2B. The anomalous Hall conductivity $\sigma_{xy}^A (= \frac{\rho_{xy}^A}{\rho_{xy}^2 + \rho_{xy}^2})$ is ~ 210 S·cm⁻¹ in sample 1, which converts to $\sim 0.122 e^2/h$ (quantum conductance) per kagome plane, comparable with top-quality TbMn₆Sn₆ crystals in literature(33). In the gapped Dirac fermion model, the Berry curvature's contribution to the anomalous Hall effect can be estimated(37) as $\sigma_{xy}^A = \frac{\Delta E}{2E_D} \times \frac{e^2}{h}$, where ΔE is the Dirac gap, and E_D is Dirac cone energy, which is $0.13 \pm 1 e^2$ (33). In Sample 2, the similar result ($0.13 e^2/h$) is also observed at room temperature, implying the Berry curvature may also contribute to an out-of-kagome plane giant anomalous Hall conductivity. The observed similar linear transport behavior in Sample 1 and Sample 2 also suggests that the electronic properties in TbMn₆Sn₆ are not affected by the FIB fabrication process. Similar behavior can be found in the 290 – 320 K region, as demonstrated in Fig. S3; the calculated anomalous Hall conductivity values are summarized in Fig. 2G. The anomalous conductivity is roughly a constant, and independent with the longitudinal conductivity, also suggesting the intrinsic (Berry curvature induced) origin.

Nonlinear transport at room temperature A frequency doubling effect was observed in the FIB-fabricated Hall bar samples by the application of an alternating current (a.c.), as shown in Fig. 2C-F for Sample 1, and Fig. S5 for Sample 2. Figs. 2 C&D shows both longitudinal and transverse second harmonic responses $\Delta V_{xx}^{2\omega}$, $\Delta V_{xy}^{2\omega}$. Note that, the second harmonic transport behavior contains two parts: 1) a magnetic-field-independent offset, and 2) the magnetic-field-dependent $\Delta V^{2\omega}$ which can be obtained via subtracting a constant offset value at $B = 0$ T. Based

on these different contributions, the nonlinear response signals have different \hat{T} -dependence, e.g., the Berry curvature dipole is a \hat{T} -even term while the Drude and quantum metric are \hat{T} -odd term.(10) Therefore, the D_{metric} -induced term can be in principle obtained via analysing the magnetic field dependence of the second harmonic transport properties. After subtracting the \hat{T} -even term of each measured curve in Sample 1, $\Delta V_{xx}^{2\omega}$, $\Delta V_{xy}^{2\omega}$ are obtained and plotted in Figs. 2 E&F. $\Delta V_{xx}^{2\omega}$ and $\Delta V_{xy}^{2\omega}$ show nonlinear behavior with magnetic field, which are odd functions and appear to saturate at sufficiently large fields. Therefore, it is highly possible that both D_{BC} and D_{metric} contribute to the nonlinear transport behavior. Further, we summarize the longitudinal and transverse nonlinear response at $B = 0, \pm 1$ T values as functions of the a.c. density (I-V) in Fig. 2 H&I, for Sample 1. The parabolic fitting curves show the current dependency of the second harmonic transport signals and clearly indicate the signature of a second-order electronic transport response. The splitting at different fields shows the tuneability in the (D_{BC} and D_{metric}) co-contribution model.

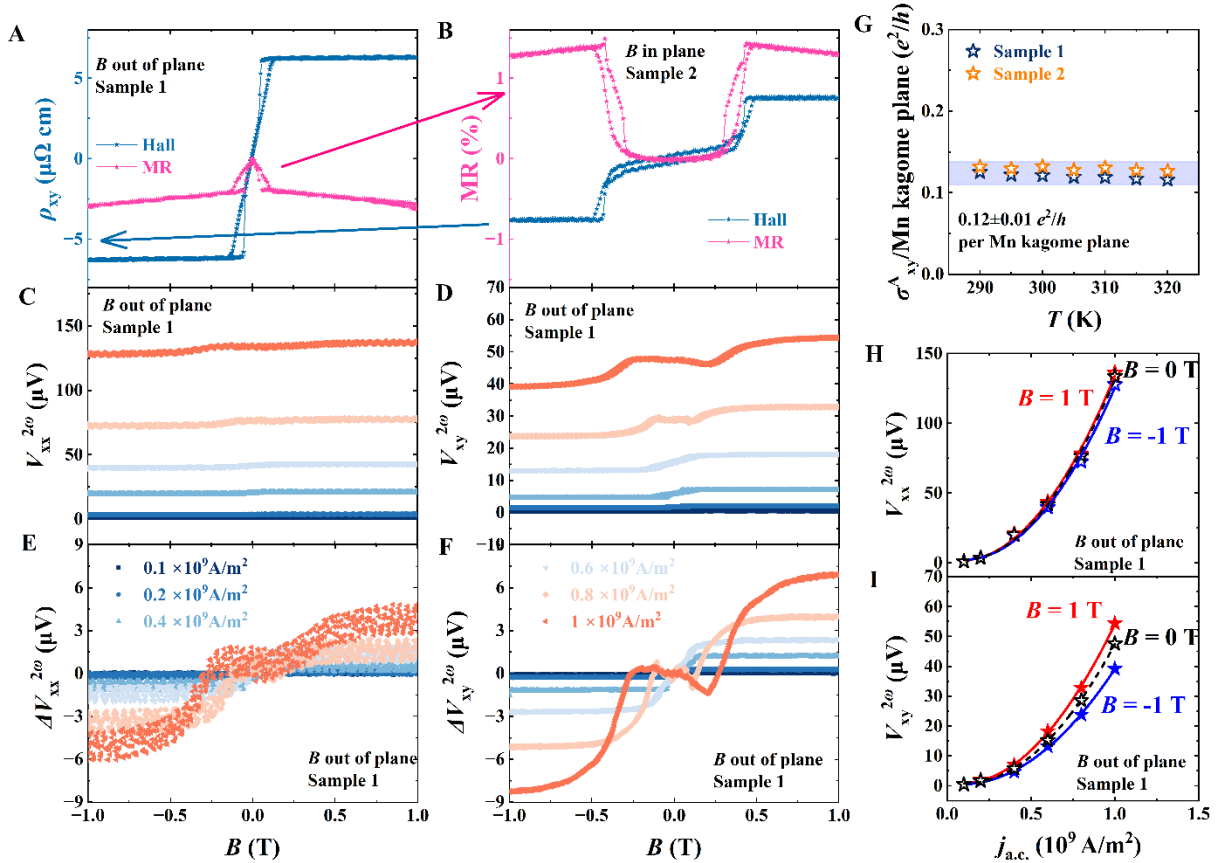


Fig. 2 The anisotropic transport properties of TbMn_6Sn_6 at 300 K. (A, B) The first order magnetotransport properties of Sample 1 and Sample 2 in $-1 - 1$ T range, in which the Hall effect of both samples are plotted in blue curve and use the blue y axis in Panel (A), the MR curves are plotted in purple and share the purple y axis in Panel (B). (C, D) The nontrivial longitudinal and transverse

second harmonic response in Sample 1 with different applied a.c. densities. (E, F) The magnetic-field dependent components in the nonlinear response shown in Panel C&D, respectively. Note that, Panel (C-F) share the same color code for current density level, which is demonstrated by the legends in Panel (E&F). (G) The Berry curvature induced anomalous Hall conductivity in 290 – 320 K region, which is converted to quantum conductance per Mn-kagome plane. (H) The longitudinal and (I) transverse second-order responses at different magnetic fields are plotted against the applied a.c. density along the a axis.

In the co-contribution model of the D_{BC} and D_{metric} , symmetry breaking is present and is induced by the in-kagome-plane antiferromagnetic alignment. As shown in Fig. 1B, with flat-band type antiferromagnetism, \hat{P} and \hat{T} are both broken, and with chiral antiferromagnetism, the \hat{T} and C_3 symmetry are broken. A nonzero quantum metric dipole D_{metric} may therefore give rise to the odd-with-magnetic-field nonlinear responses, on top of the magnetic-field-even components contributed by D_{BC} . In contrast with sample 1, the responses in Sample 2 are substantially weaker and exhibit a different field dependence (Fig. S5), implying these nonlinear responses originate from the magnetic configurations. To understand these differences the contribution to the signal from the spin reorientation was probed as a function of temperature, magnetic field and a.c. density dependent measurements.

Spin reorientation, chirality and Skyrmions The SR is triggered by an increase in the Tb single ion anisotropy energy with cooling (15, 31), which favours the c axis and consequently forces the Mn moments to rotate in the antiparallel ($-c$ in this case) direction. Since the spontaneous T_{SR} is near room temperature, an applied magnetic field will also easily alter the spin configuration in this temperature range. Although the nonlinear transport is insignificant when the magnetic field is applied in the basal plane (Sample 2) compared with B along the c -axis, peaks in $\Delta V_{xy}^{2\omega}$ with $\sim 40\%$ intensity of Sample 1 maximum are observed around the field-induced SR region in sample 2 (Fig. S5). To directly compare, the field-dependent second harmonic Hall effect components (see Supplementary Figs. S6 & S7 for details) are plotted into a four-dimensional color map in Fig. 3A. Low field features (indicated with a purple arrow), which are approximately the same intensity appear in both sample 1 and 2 (e.g. B applied out of basal plane and in basal plane, respectively). These features appear at different temperatures depending on the sample and are consistent with a field-driven spin reorientation.

To further study the nonlinear response from the spin reorientation, Fig. 3B shows a plot of $V_{SR}^{2\omega}$, which is the SR-related second harmonic Hall component (see SI for $V_{SR}^{2\omega}$ calculation and its temperature, magnetic field and a.c. density dependency). As shown in Fig. 3B, the

“peak” values ($\sim 4.5 \mu\text{V}$ for Sample 1 and $\sim 3.5 \mu\text{V}$ for Sample 2) at 305 K for both samples are comparable, indicating a similar underlying 3D-like mechanism. In Fig. 3A, a naïve model demonstrates the nominal spin configuration. Recent neutron scattering experiments (16, 31, 38) suggest that on top of the long-range ferromagnetic ordering in the Mn kagome layers, antiferromagnetic chiral magnons exist. Our magnetic study (Fig. S2) also suggests the robust in-kagome-plane moment components in the studied region, which is necessary for the presence of in-plane antiferromagnetism. Moreover, experimental observations (28, 39) of Skyrmions and electrical control of these chiral magnetic structures has been demonstrated. Further, the antiferromagnetic chiral magnons contain in-plane and out-of-plane components (31), which support 3D Skyrmion dynamics, and thus contribute to the 3D-like behaviour in Fig. 3B. Therefore, TbMn_6Sn_6 is a chiral magnet which could give rise to a strong eMChA effect in the second harmonic Hall response.

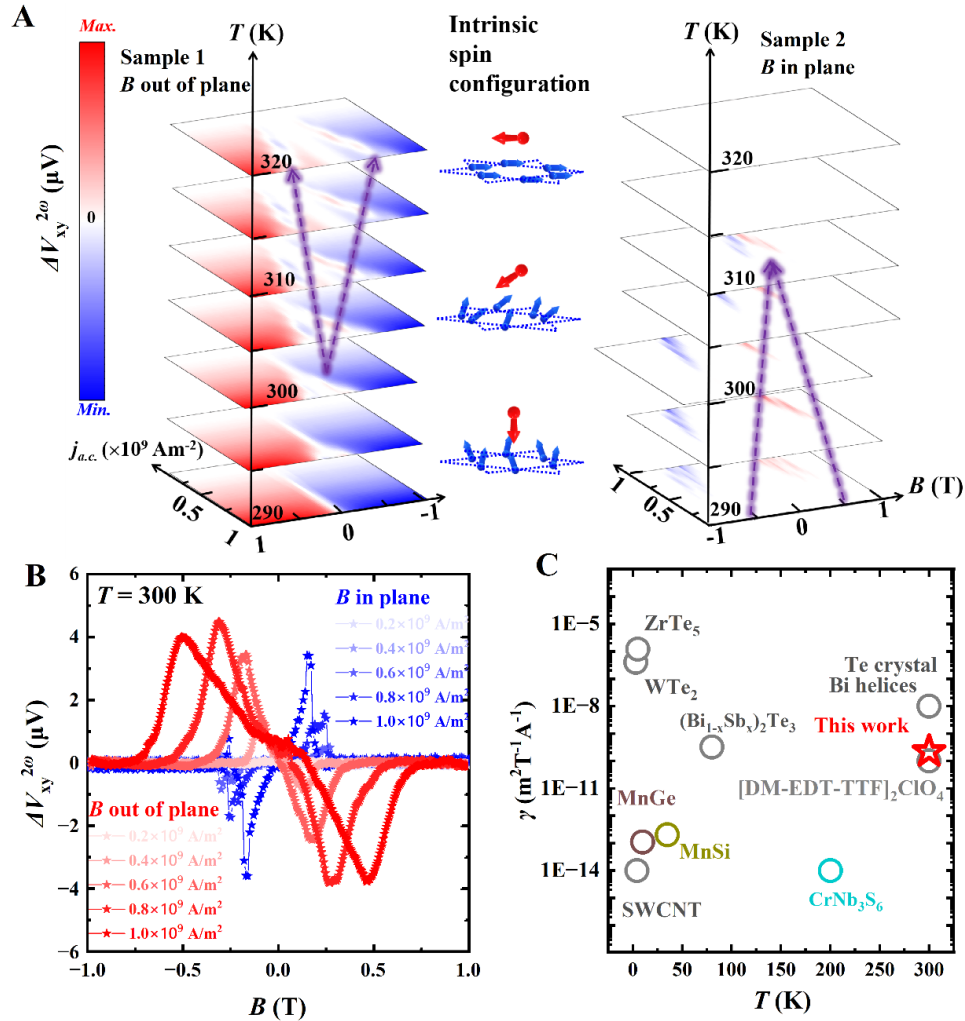


Fig. 3 Second harmonic transport in TbMn_6Sn_6 . (A) The magnetic field dependent components of second harmonic Hall effect ($\Delta V_{xy}^{2\omega}$) in Sample 1 and Sample 2 are summarized in 4D color map, in

which the temperature-, magnetic field-, a.c. density- axes, as well as the color code are all in the same scale for both samples. The purple arrows indicate the field induced spin reorientation transition. The schematic in Panel A, indicating the spontaneous spin orientation transition, shows the nominal spin configurations at 320, 310 and 290 K (top - down), in which the red and blue arrows indicate Tb and Mn moments, respectively. Note that, large external fields will induce the reorientation transitions, and force the moments mostly align along the applied fields. (B) The second harmonic Hall voltage related to the chiral magnetic structure. (C) The electric magnetochiral anisotropy coefficients from some popular quantum materials(40-48) are summarized at different temperatures, in which the room-temperature maximum value observed in TbMn₆Sn₆ is highlighted. Note that, the non-tuneable compounds are plotted in grey circles, and the materials that show tuneable nonlinear transport behavior are plotted using different colors.

Discussion and Conclusion Based on these results, there are clearly two distinct mechanisms that contribute to the large field-dependent nonlinear response near room temperature. The first is the eMChA effect arising from the field-induced spin reorientation of the chiral magnetic structure around the spin reorientation temperature. Due to the three-dimensional nature of the Skyrmions (real-space topology) in this material, the effect is observed with both out-of- and in-kagome plane applied fields. The second contribution is from the electronic band structure (D_{metric} and D_{BC}), which arises only when $B // c$ (Fig. S9). This result can be understood by considering the symmetry in the material.

The quantum metric can arise in a material with broken \hat{P} and broken \hat{T} symmetry. The symmetry breaking depends on in-plane antiferromagnetism, and is supported by a slight canting of the moments ($\sim 13^\circ$). (24) Therefore, this broken \hat{P} and broken \hat{T} symmetry is only present when $B // c$ -axis. When $B //$ basal plane, the parallel alignment of the Mn moments in the kagome lattice will no longer break \hat{P} symmetry, and thus only Skyrmion-induced components are observed in Sample 2. In this scenario, the nonlinear response can be easily controlled via changing temperatures or applied fields in room temperature region.

A significant room temperature nonlinear response is a key requirement in designing highly-efficient nonlinear devices. Recently, a large D_{BC} has been demonstrated using second harmonic transport at room temperature in topological materials such as the Weyl semimetal TaIrTe₄(49), the Dirac semimetal BaMnSb₂(43), and Bi thin films(50). In addition to room temperature operation, a key requirement for emerging devices is tuneability, which has been reported in a symmetry breaking phase in the Kagome CsV₃Sb₅ compound, although only at cryogenic temperatures (12). In Fig. 3C, the coefficient of eChMA, $\gamma = 4V^{2\omega}/(V^\omega B j_{a.c.})$ in

some popular materials are summarized, together with our work on TbMn_6Sn_6 . Among all of the materials, TbMn_6Sn_6 is the only one which demonstrates giant, tuneable second harmonic transport behavior at room-temperature.

We have shown that in TbMn_6Sn_6 , the Berry curvature dipole, quantum metric dipole and Skyrmion induced second harmonic transport behavior coexist at room temperature, and can be tuned via control of the magnetic configurations. The giant and tuneable effect is confirmed in multiple samples, thus promoting a room temperature controllable response of the nonlinear physics for device design. The rich physics of kagome materials may prove a fertile playground to identify other quantum metric driven non-linear responses, which could open a new direction in practical nonlinear device design for next-generation electronics and spintronics.

Acknowledgements This work is supported by ARC Centre of Excellence in Future Low-Energy Electronics Technologies No. CE170100039, Australian Research Council Discovery Project DP200102477, DP220103783, the National Natural Science Foundation of China No. 12174039. This work was performed in part at the Melbourne Centre for Nanofabrication (MCN) in the Victorian Node of the Australian National Fabrication Facility (ANFF). The FIB fabrications are conducted in Monash Centre for Electron Microscope (MCEM).

1. Y. Tokura, N. Nagaosa, Nonreciprocal responses from non-centrosymmetric quantum materials. *Nature communications* **9**, 3740 (2018).
2. Q. Ma *et al.*, Observation of the nonlinear Hall effect under time-reversal-symmetric conditions. *Nature* **565**, 337-342 (2019).
3. H. Isobe, S.-Y. Xu, L. Fu, High-frequency rectification via chiral Bloch electrons. *Science advances* **6**, eaay2497 (2020).
4. Y. Zhang, L. Fu, Terahertz detection based on nonlinear Hall effect without magnetic field. *Proceedings of the National Academy of Sciences* **118**, e2100736118 (2021).
5. Z. Du, H.-Z. Lu, X. Xie, Nonlinear hall effects. *Nature Reviews Physics* **3**, 744-752 (2021).
6. D. Kaplan, T. Holder, B. Yan, Unification of nonlinear anomalous Hall effect and nonreciprocal magnetoresistance in metals by the quantum geometry. *Physical review letters* **132**, 026301 (2024).
7. K. Kang, T. Li, E. Sohn, J. Shan, K. F. Mak, Nonlinear anomalous Hall effect in few-layer WTe_2 . *Nature materials* **18**, 324-328 (2019).
8. A. Gao *et al.*, Quantum metric nonlinear Hall effect in a topological antiferromagnetic heterostructure. *Science* **381**, 181-186 (2023).

9. N. Wang *et al.*, Quantum-metric-induced nonlinear transport in a topological antiferromagnet. *Nature* **621**, 487-492 (2023).
10. Y. Michishita, N. Nagaosa, Dissipation and geometry in nonlinear quantum transports of multiband electronic systems. *Physical Review B* **106**, 125114 (2022).
11. T. Ideue *et al.*, Bulk rectification effect in a polar semiconductor. *Nature Physics* **13**, 578-583 (2017).
12. C. Guo *et al.*, Switchable chiral transport in charge-ordered kagome metal CsV₃Sb₅. *Nature* **611**, 461-466 (2022).
13. R. Khasanov *et al.*, Time-reversal symmetry broken by charge order in CsV₃Sb₅. *Physical Review Research* **4**, 023244 (2022).
14. C. Mielke III *et al.*, Time-reversal symmetry-breaking charge order in a kagome superconductor. *Nature* **602**, 245-250 (2022).
15. S. X. M. Riberolles *et al.*, Low-Temperature Competing Magnetic Energy Scales in the Topological Ferrimagnet TbMn₆Sn₆. *Phys. Rev. X* **12**, 12 (2022).
16. S. Riberolles *et al.*, Chiral and flat-band magnetic quasiparticles in ferromagnetic and metallic kagome layers. *Nature Communications* **15**, 1592 (2024).
17. S.-C. Ho *et al.*, Hall effects in artificially corrugated bilayer graphene without breaking time-reversal symmetry. *Nature Electronics* **4**, 116-125 (2021).
18. M.-S. Qin *et al.*, Strain tunable Berry curvature dipole, orbital magnetization and nonlinear Hall effect in WSe₂ monolayer. *Chinese Physics Letters* **38**, 017301 (2021).
19. M. Huang *et al.*, Giant nonlinear Hall effect in twisted bilayer WSe₂. *National Science Review* **10**, nwac232 (2023).
20. P. He *et al.*, Graphene moiré superlattices with giant quantum nonlinearity of chiral Bloch electrons. *Nature nanotechnology* **17**, 378-383 (2022).
21. M. Brooks, L. Nordström, B. Johansson, Rare-earth transition-metal intermetallics. *Physica B: Condensed Matter* **172**, 95-100 (1991).
22. W. L. Ma *et al.*, Rare Earth Engineering in RMn₆Sn₆ (R = Gd-Tm, Lu) Topological Kagome Magnets. *Physical Review Letters* **126**, 5 (2021).
23. X. T. Xu *et al.*, Topological charge-entropy scaling in kagome Chern magnet TbMn₆Sn₆. *Nature Communications* **13**, 7 (2022).
24. B. C. Elidrissi, G. Venturini, B. Malaman, D. Fruchart, MAGNETIC-STRUCTURES OF TbMn₆Sn₆ AND HoMn₆Sn₆ COMPOUNDS FROM NEUTRON-DIFFRACTION STUDY. *Journal of the Less-Common Metals* **175**, 143-154 (1991).
25. L. L. Gao *et al.*, Anomalous Hall effect in ferrimagnetic metal RMn₆Sn₆ (R = Tb, Dy, Ho) with clean Mn kagome lattice. *Appl. Phys. Lett.* **119**, 5 (2021).
26. G. H. Guo, H. B. Zhang, The spin reorientation transition and first-order magnetization process of TbMn₆Sn₆ compound. *J. Alloy. Compd.* **448**, 17-20 (2008).
27. Y. Lee *et al.*, Interplay between magnetism and band topology in the kagome magnets RMn₆Sn₆. *Physical Review B* **108**, 13 (2023).
28. Z. L. Li *et al.*, Discovery of Topological Magnetic Textures near Room Temperature in Quantum Magnet TbMn₆Sn₆. *Adv. Mater.* **35**, 9 (2023).
29. C. Mielke *et al.*, Low-temperature magnetic crossover in the topological kagome magnet TbMn₆Sn₆. *Commun. Phys.* **5**, 9 (2022).
30. X. B. Qiang, Z. Z. Du, H. Z. Lu, X. C. Xie, Topological and disorder corrections to the transverse Wiedemann-Franz law and Mott relation in kagome magnets and Dirac materials. *Physical Review B* **107**, 6 (2023).
31. S. X. M. Riberolles *et al.*, Orbital character of the spin-reorientation transition in TbMn₆Sn₆. *Nature Communications* **14**, 8 (2023).

32. M. Wenzel *et al.*, Effect of magnetism and phonons on localized carriers in the ferrimagnetic kagome metals GdMn₆Sn₆ and TbMn₆Sn₆. *Physical Review B* **106**, 7 (2022).
33. J. X. Yin *et al.*, Quantum-limit Chern topological magnetism in TbMn₆Sn₆. *Nature* **583**, 533 (2020).
34. H. D. Zhang *et al.*, Exchange-biased topological transverse thermoelectric effects in a Kagome ferrimagnet. *Nature Communications* **13**, 8 (2022).
35. B. Raquet, M. Viret, E. Sondergard, O. Cespedes, R. Mamy, Electron-magnon scattering and magnetic resistivity in 3d ferromagnets. *Physical Review B* **66**, 024433 (2002).
36. L. Wang *et al.*, Orbital magneto-nonlinear anomalous Hall effect in kagome magnet Fe₃Sn₂. *Physical Review Letters* **132**, 106601 (2024).
37. N. Sinitsyn, A. MacDonald, T. Jungwirth, V. Dugaev, J. Sinova, Anomalous Hall effect in a two-dimensional Dirac band: The link between the Kubo-Streda formula and the semiclassical Boltzmann equation approach. *Physical Review B* **75**, 045315 (2007).
38. Z. Huang *et al.*, Microscopic origin of the spin-reorientation transition in the kagome topological magnet TbMn₆Sn₆. *Physical Review B* **109**, 014434 (2024).
39. Z. Li *et al.*, Electron-Assisted Generation and Straight Movement of Skyrmion Bubble in Kagome TbMn₆Sn₆. *Adv. Mater.*, 2309538 (2024).
40. G. Rikken, J. Fölling, P. Wyder, Electrical magnetochiral anisotropy. *Physical review letters* **87**, 236602 (2001).
41. G. Rikken, N. Avarvari, Strong electrical magnetochiral anisotropy in tellurium. *Physical Review B* **99**, 245153 (2019).
42. Y. Wang *et al.*, Gigantic magnetochiral anisotropy in the topological semimetal ZrTe₅. *Physical Review Letters* **128**, 176602 (2022).
43. L. Min *et al.*, Strong room-temperature bulk nonlinear Hall effect in a spin-valley locked Dirac material. *Nature communications* **14**, 364 (2023).
44. T. Yokouchi, Y. Ikeda, T. Morimoto, Y. Shiomi, Giant Magnetochiral Anisotropy in Weyl Semimetal WTe₂ Induced by Diverging Berry Curvature. *Physical Review Letters* **130**, 136301 (2023).
45. V. Krstić, S. Roth, M. Burghard, K. Kern, G. Rikken, Magneto-chiral anisotropy in charge transport through single-walled carbon nanotubes. *The Journal of chemical physics* **117**, 11315-11319 (2002).
46. F. Pop, P. Auban-Senzier, E. Canadell, G. L. Rikken, N. Avarvari, Electrical magnetochiral anisotropy in a bulk chiral molecular conductor. *Nature Communications* **5**, 3757 (2014).
47. A. Kitaori *et al.*, Enhanced electrical magnetochiral effect by spin-hedgehog lattice structural transition. *Physical Review B* **103**, L220410 (2021).
48. H. F. Legg *et al.*, Giant magnetochiral anisotropy from quantum-confined surface states of topological insulator nanowires. *Nature Nanotechnology* **17**, 696-700 (2022).
49. D. Kumar *et al.*, Room-temperature nonlinear Hall effect and wireless radiofrequency rectification in Weyl semimetal TaIrTe₄. *Nature Nanotechnology* **16**, 421-425 (2021).
50. P. Makushko *et al.*, A tunable room-temperature nonlinear Hall effect in elemental bismuth thin films. *Nature Electronics*, 1-9 (2024).